nature communications

Article

https://doi.org/10.1038/s41467-025-64596-4

Ligand-exchange-assisted printing of colloidal nanocrystals to enable all-printed sub-micron optoelectronics

Received: 20 October 2024

Accepted: 18 September 2025

Published online: 16 October 2025

Check for updates

Zhixuan Zhao[1], Ran An[1], Yu Liu[2], Byung Ku Jung[3], Jun Hyuk Ahn[3], Ni Yang[2], Guodan Wei[4], Wallace C. H. Choy[1,5], Lain-Jong Li[2], Soong Ju Oh[3], Ji Tae Kim[2,6] ✉ & Tianshuo Zhao[1,5] ✉

Additive manufacturing enables customised device fabrication for emerging sensing technologies. However, printable (opto)electronic devices with sophisticated architectures, including all-printed photodiodes, face challenges in multi-material and multi-layer printing at micro- and nanoscales with low processing temperatures. Herein, we establish a nano-resolution printing method based on electrohydrodynamic printing (EHDP) to deposit inks from the colloidal nanocrystal (NC) library, followed by in situ room-temperature ligand exchange to functionalise the NC solids. This general approach enables layer-by-layer printing with wide selections of NC inks, ligand reagents, substrates, and device architectures. Chemical-treatment-induced contraction and densification grants printed Ag NC structures electrical conductivity and an achievable feature size and filling ratio of 70 nm and 75%, respectively, constructing wide-gamut structural colour gratings. By exploiting Ag, Au, PbS, and ZnO NCs and compact ligands, we demonstrate all-printed multi-layer infrared photodiodes with sub-10-μm pixel sizes. The nano-printing assembly of hetero-NCs promises the facile integration of multi-functional micro-nano devices.

Ubiquitous sensing and computing are becoming realistic with the rapid advancement of Internet of Things (IoT) networks, wearable technologies, autonomous machines, and AR/VR devices. Central to these technologies are integrated microelectronic sensors and detectors, whose size, form factor, and device characteristics must adapt to application-specific requirements[1,2]. For instance, different types of infrared (IR) photodetectors with tailored characteristics are needed for distinct applications, such as motion sensing in auto-driving vehicles, environmental monitoring via IoT technologies, and biomarker detection in wearable healthcare devices. Therefore, on-demand manufacturing offers a scalable and cost-effective solution, allowing the assembly of multi-material components with engineered properties to realise diverse device functionalities. Additive manufacturing, also known as 3D printing, is one promising approach to fabricating customised device structures at multiscale with desirable ink materials[3,4]. Although stereolithography and two-photon polymerisation-based 3D printing have achieved sub-micron resolution and geometrical complexity, the inks are still limited to metal(oxide)s and polymeric materials, and the final products typically serve machinal and optical applications[5,6]. Fully printed microelectronics have been limited in structural and functional diversity. The printing resolution, uniformity, and precision control of material properties can still be improved[7,8]. For efficient IR photodetection, patterning and functionalising of semiconductor inks with various/tunable bandgaps has

[1]Department of Electrical and Electronic Engineering, The University of Hong Kong, Hong Kong SAR, China. [2]Department of Mechanical Engineering, The University of Hong Kong, Hong Kong SAR, China. [3]Department of Materials Science and Engineering, Korea University, Anam-Dong, Seongbuk-Gu, Seoul, Republic of Korea. [4]Institute of Materials Research, Tsinghua Shenzhen International Graduate School-Tsinghua University, Shenzhen, China. [5]Materials Innovation Institute for Life Sciences and Energy (MILES), HKU-SIRI, Shenzhen, PR China. [6]Department of Mechanical Engineering, Korea Advanced Institute of Science and Technology (KAIST), Daejeon, Republic of Korea. ✉e-mail: jitae.kim@kaist.ac.kr; tszhao@hku.hk

been rarely reported[9]. Printing the whole multi-layer device stacks like metal contacts/transport layers/photo-absorbing layers (PN or PIN junctions)/transport layers/metal contacts is also not yet achieved[10].

To address these major challenges, it is necessary to cohesively establish a widely tunable ink system and a versatile printing-sintering mechanism. Colloidal nanocrystals (NCs) serve as ideal ink materials for printed electronics, as their successful device integration has been demonstrated in integrated/flexible circuits, photodetectors, and photovoltaics using cost-effective solution processing methods[11,12]. NCs comprise nanocrystalline cores encapsulated by ligand shells, showing a broad range of designable material properties. The semiconductive family of NCs is also known as quantum dots (QDs) and prized for size-dependent optoelectronic properties[13]. To facilitate carrier transport in NC-based electronic devices, ligand-exchange (L-E) is typically performed to replace or remove the insulating long-chain organic ligands on the NC surface by compact ligands and enable electronic coupling of NC arrays[12]. Selective ligand reagents further modify carrier mobility and lifetime, doping type and concentration, and energy level positions of NC ensembles to construct complex device architectures through layer-by-layer coating of NCs[14]. The multi-layer deposition strategy is also reported to fill and smooth micron-size voids and cracks caused by organic ligand volume loss during the solid-state L-E process.

Recently, 3D-printed NC and nanoparticle structures have entered nanoscale resolution through various external field-assisted assembly methods. For instance, the flow field and predefined electric field direct charged metal particles to construct 3D nanostructures[15,16]. Laser-induced hydrogel polymerisation and sintering mechanically assemble metal nanoparticles to achieve a linewidth as low as 20 nm[17]. Two-photon-induced near-field optical forces enhance rapid precursor decomposition, assembly, and sintering of metal atoms to enable 100-nm metal and metal oxide structures[18]. Photosensitive ligand linkage of NCs upon two-photon initiation drives local self-assembly, enlarging the pool of printing-patternable inorganic NC inks[19]. However, these examples still rely on particular NC types and/or ligand matrices, facing difficulties fulfilling the full range of tunable physical properties offered by metal, semiconductor, and dielectric NCs for solid-state device construction.

Electrohydrodynamic printing (EHDP) supports a variety of ink materials from metal to semiconductor and metal oxide nanoparticles, and ultrahigh printing resolution to nanoscale beyond the limitation of nozzle diameters[20]. However, the remaining organic ligands and stabilisers in the as-printed structures, e.g., from Au and Ag inks[21–23], require to be removed by annealing above 150 °C. This post-processing can deteriorate some semiconductive NCs, especially unstable IR-absorbing PbS and HgTe NCs, and flexible substrates of low thermal resistance during multi-material printing. Combined with low-temperature post-printing chemical treatment, EHDP has also been reported to deposit semiconductive NCs (or QDs) as sensitisers on graphene for enhancing infrared (IR) photodetection[24,25]. However, to achieve more scalable all-printed NC optoelectronic devices, mechanistic studies are still lacking in fine-tuning the NC-surface ligand interplay during EHDP and enabling multi-layer printing.

Herein, we report an L-E-assisted EHDP strategy to assemble sub-micron NC structures followed by onsite room-temperature chemical modification and functionalisation, enabling layer-by-layer printing of NC microelectronic devices. The generality of this method is showcased by two model NC systems, namely Ag NCs and PbS NCs, in combination with a series of ligand reagents. Upon the L-E process with compact ligands, the printed NC patterns undergo contraction and densification, reducing the printed linewidth to as low as 70 nm for Ag NCs on Si substrates and improving electrical conductivity across the NC array. We explore EHDP parameters to assemble continuous nano-lines of Ag NCs and fabricate wide-gamut structure colour gratings, sub-micron electrode arrays, and split-ring metasurfaces on both Si/SiO_2 and polymer substrates. These nano-lines are further densely packed to form high-filling-ratio and crack-free micron-size films. By analysing the localised IR spectra and morphology evolution, we study the dynamic interaction between NCs and ligands during the EHDP process to facilitate L-E-induced grain growth of printed Ag NC films. The resulting Ag NC micron-size films achieve a high DC conductivity of 1.99×10^7 S/m with the NH_4SCN ligand treatment. Finally, PbS NC micron-size films are printed with iodide and thiol group L-E treatment and show optoelectronic properties comparable to those of the spin-coated ones. We integrate these semiconductor NCs and n- and p-doping L-E treatment through multi-layer and multi-ink printing, successfully showing all-printed PbS NC/ZnO NC IR photodiodes at a sub-10-μm pixel size. They operate at lower dark currents and faster photoresponse than the printed PbS NC photoconductors under 1480 nm illumination.

Results

Mechanisms of L-E assisted nano-printing of NC assemblies

Colloidal NCs are typically synthesised with long organic capping ligands, forming stable inks for EHDP processes. As shown in Fig. 1a, various NC core materials, including metals, semiconductors (also known as QDs), and metal oxides, are prepared with oleic acid (OA) or oleylamine (OLAM) surface ligands and well dispersed in non-polar solvents like dodecane (see "Methods"). They are deposited by EHDP following previously reported nanoscale dynamics[20], where the electric force generated by pulsed voltages is sufficient to overcome the surface tension and viscous force of the ink and eject droplets from the meniscus at the nozzle tip. As illustrated in Fig. S1, by moving the stage of the home-built EHD printer along one direction, we print the NCs into lines on the substrate (Fig. 1b). These printed lines, as basic elements, can be further arranged and combined to create on-demand patterns and thin films with arbitrary shapes by programming the stage trajectories.

These as-printed NC structures, however, are electrically insulating due to the separation of individual NCs by bulky organic ligands (Fig. 1a). Therefore, we introduce compact ligand reagents, such as ethanedithiol (EDT), NH_4SCN, tetrabutylammonium iodide (TBAI), and PbI_2 dissolved in polar solvents to displace the long organic molecules (Fig. 1e). Akin to the solid-state ligand exchange (L-E) treatment used in large-area NC thin films, solutions containing compact ligands are applied to cover the entire printed structures for 30–120 s followed by excessive rinsing steps (Fig. 1c). As a result of the L-E process, the interparticle distance is greatly shortened by removing or replacing the long ligands with the compact ligands. These chemical reactions are thermodynamically favourable and thus do not require elevated temperatures. Due to the large volume loss and change of NC surface energy during the post-printing L-E process, NCs are driven to rearrange and even partially fuse in the printed ensembles, leading to an observable structural change as well as physical property modification (Fig. 1d). We choose Ag NC inks and the NH_4SCN L-E treatment as model systems to further investigate the mechanism of the L-E-assisted EHDP method.

We verify the effectiveness of using a 1 mg/ml concentration for the NH_4SCN L-E treatment on EHD-printed Ag NCs by the nano-FTIR technique (Fig. S2)[26,27]. We print an OA-capped Ag NC layer to partially cover a printed and NH_4SCN-exchanged Ag NC layer, such that their morphologies and IR spectra can be compared side-by-side. The colour contrast in the scanning electron microscopy (SEM) image reflects the difference in conductivity and z-height of the two areas of printed Ag NC films (Fig. 1f), whereas the nano-FTIR image indicates their drastically different intensities of IR absorption at 2900 cm^{-1} wavenumber (Fig. 1g). In Fig. 1h, the FTIR absorption collected locally from the as-printed Ag NC film and the L-E treated Ag NC film shows that the C-H stretch for organic ligand signatures thoroughly disappears after

https://doi.org/10.1038/s41467-025-64596-4

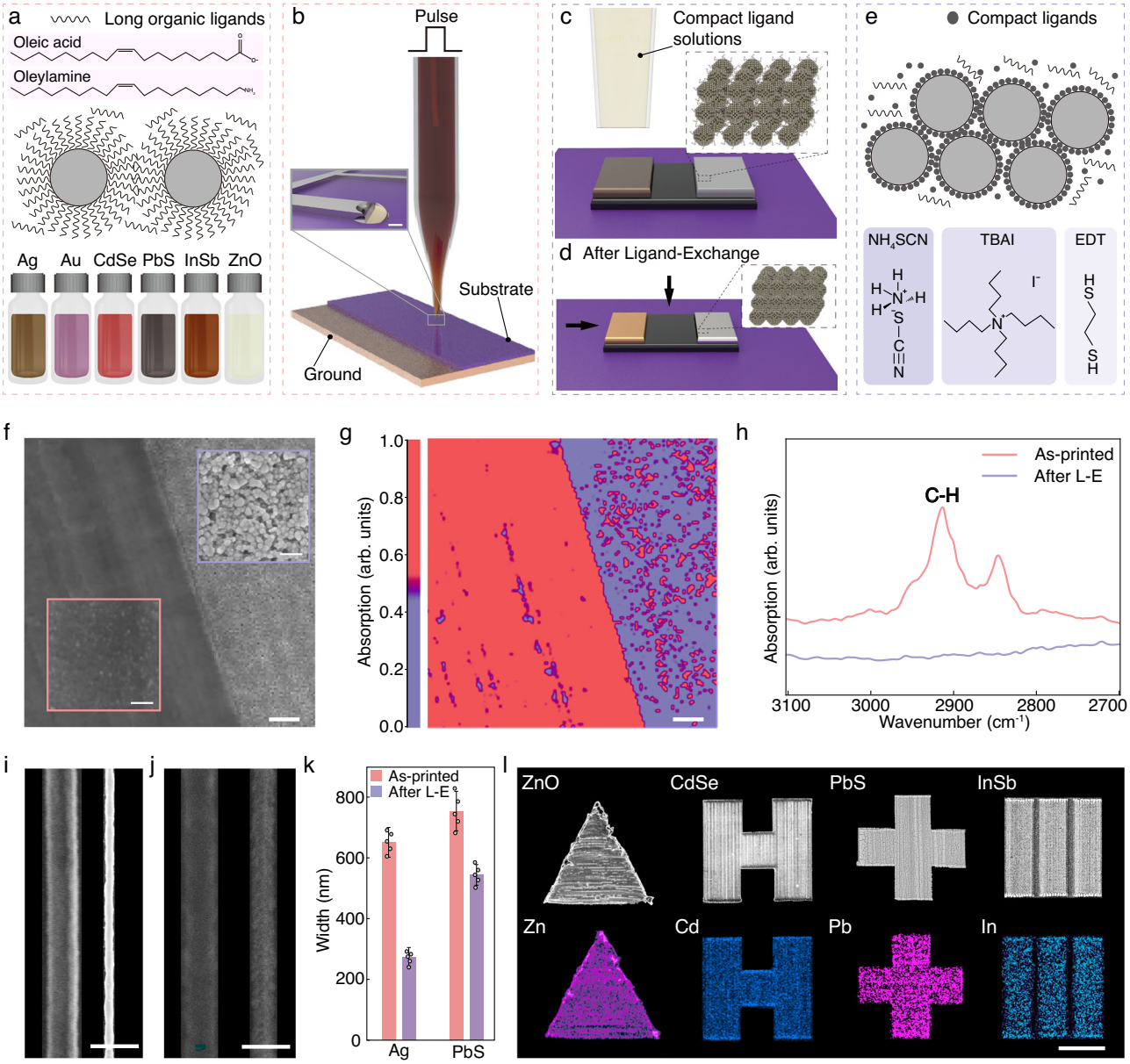

Fig. 1 | Ligand-exchange (L-E)-assisted nano-printing of nanocrystals (NCs). **a** Schematics of as-synthesised NCs capped by organic ligands and their dispersions as printable inks with their compositions. **b** Illustration of the electrohydrodynamic printing (EHDP) process for depositing NC inks. Scale bar: 20 nm. Schematics of **c** the in situ L-E process and **d** L-E-induced morphology change of NC patterns (with arrows indicating the shrinking directions) and L-E-assisted nano-printing of multi-layer and multi-material in different colours. **e** Schematics of closely packed NCs after L-E with various compact ligand reagents. **f** SEM images of as-printed Ag NCs film (left) deposited on top of NH_4SCN-treated printed Ag NC film (right). Scale bars: 1 µm in the main image and 200 nm in the enlarged image. **g** Nano-FTIR mapping of the same area as **f** for the normalised absorption intensity at 2900 cm^{-1} wavenumber of the same area. Scale bar: 1 µm. **h** Representative nano-FTIR absorption spectra taken in the as-printed (left) and L-E-treated (right) regions of (**g**). **i** SEM images of a representative Ag NC line as printed (left) and after the NH_4SCN L-E treatment (right). Scale bar: 1 µm. **j** SEM images of a representative PbS NC line as printed (left) and after the TBAI L-E treatment (right). Scale bar: 1 µm. **k** Width of these printed Ag and PbS NC lines in **i** and **j** to compare the dimension reduction after L-E. (Error bars represent standard deviation of $n = 5$ independent measurements.) **l** SEM images (top) and EDX elemental mappings (bottom) of printed ZnO, CdSe, PbS, and InSb NC patterns of different geometries treated by the NH_4SCN or EDT L-E process. Scale bar: 15 µm.

the NH_4SCN treatment. Therefore, the L-E reaction is complete using 1 mg/mL NH_4SCN solutions, leading to inversion of the NC surface chemistry from non-polar to polar. Such orthogonal surface polarity minimises the redissolution during successive deposition of NC layers, ensuring sharp edges of the Ag NC layer printed on top of the NH_4SCN-treated Ag NC layer (Fig. 1f, g). This layer-by-layer printing with alternative NC deposition and L-E treatment grows the film thickness in building multi-layer stacks (Fig. 1d). It is noted that spots with high FTIR absorption still exist on the ligand-exchanged Ag NC layer, which coincide with the voids formed due to the L-E (Fig. S2) that expose the self-assembled monolayer coated on the Si substrate underneath the Ag NC film.

Under the L-E condition of 1 mg/mL NH_4SCN or TBAI solution and 60 s treatment time, we observe the volume shrink and linewidth reduction of printed NC lines. For example, the width of printed Ag NC lines is reduced from 651 ± 49 nm to 274 ± 31 nm after the NH_4SCN L-E, while the as-printed PbS NC lines shrink from 754 ± 65 nm to 544 ± 34 nm after the TBAI ligand exchange (Fig. 1i–k). The difference in length between OA and NH_4SCN or TBAI ligands accounts for approximately 1 nm reduction of the interparticle distance, equivalent

https://doi.org/10.1038/s41467-025-64596-4

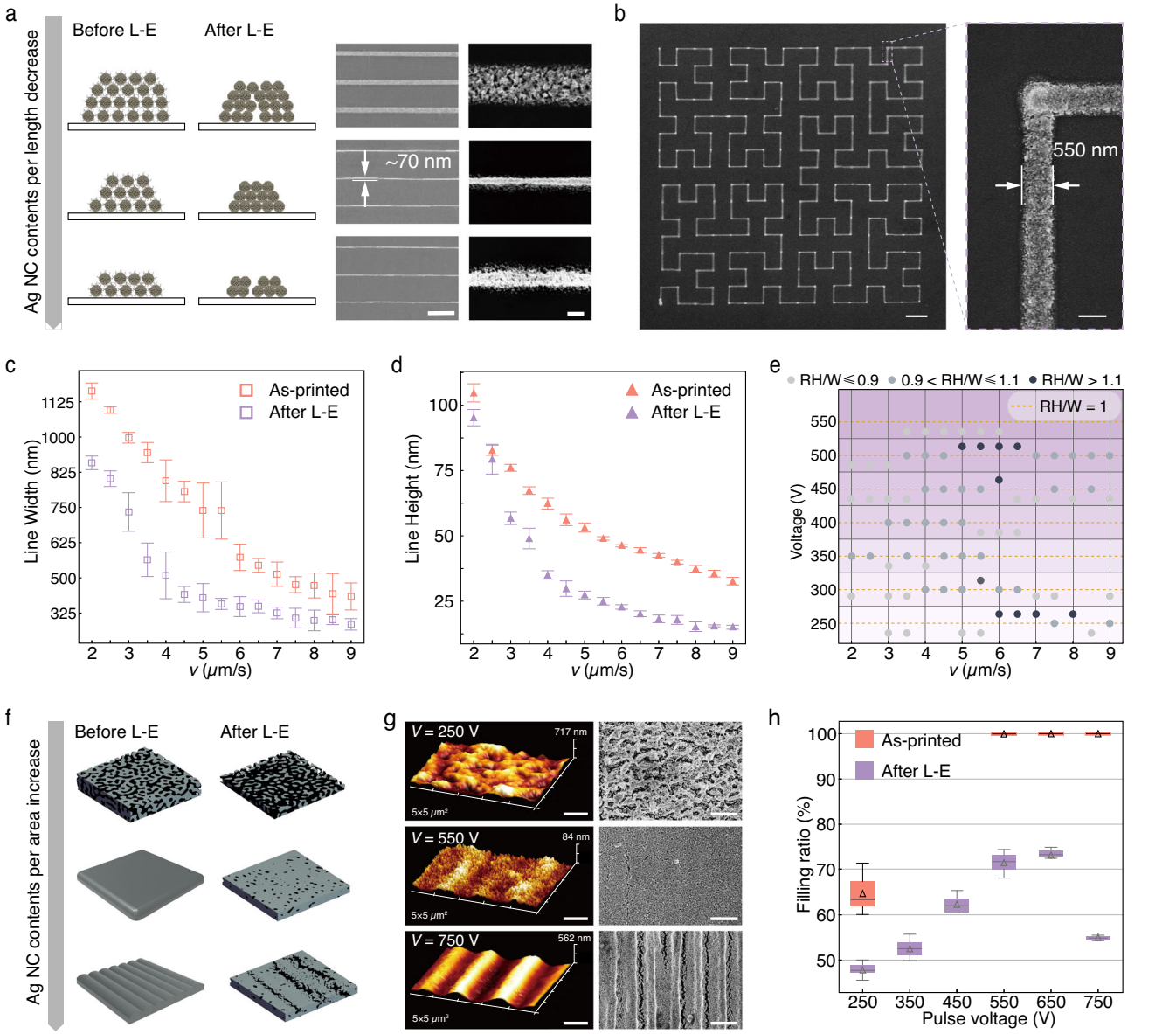

Fig. 2 | Combined effect of printing parameters and the L-E treatment on morphologies of Ag NC patterns. a Shrinking mechanisms of Ag NC lines printed with different amount of NCs deposited per unit length and underwent the NH_4SCN L-E process, and corresponding low- (left) and high-magnification (right) SEM images. Scale bars: 5 μm (left) and 200 nm (right). **b** Low-(left) and high -(right) magnification SEM images of printed Ag NC Hilbert curves after the NH_4SCN L-E treatment. Scale bars: 5 μm (left) and 500 nm (right). **c** Width and **d** height of Ag NC lines printed under 350 V pulse voltage and various printing speeds before (pink) and after (purple) the same NH_4SCN L-E treatment. (Error bars in both **c** and **d** represent the standard deviation of $n = 5$ independent measurements.) **e** The aspect ratio (height/width, or H/W) of printed Ag NC lines after L-E relative to that before L-E (RH/W) under different printing speeds v and pulse voltages V. The darkness of the dots corresponds to the value of the RH/W. Cases with RH/W below 0.8 are omitted from the plot. **f** Schematics of printed Ag NC films with low (top row), medium (middle row), and high (bottom row) pulse voltages V before (left) and after (right) the NH_4SCN treatment. **g** AFM images (left) of Ag NC films printed with various pulse voltages V and SEM images (right) after the NH_4SCN L-E treatment. Scale bars: 1 μm (left) and 2 μm (right). **h** The filling ratio (FR) of Ag NC films printed at various V before (pink) and after (purple) the NH_4SCN L-E treatment. (Error bars represent $n = 15$ independent measurements. The triangular symbol represents the average value of the sample, and the line in the middle of the box represents the median of the sample. The upper and lower box boundaries represent the upper and lower quartiles. The upper and lower error bars represent the maximum and minimum values from the measured samples).

to 20% of the particle diameter. More significant shrinking of the printed Ag NC microstructures is attributed to further densification of Ag NCs through NC sintering and local grain growth during the L-E treatment, a process known as chemical sintering of metal NCs[28,29]. The L-E-induced NC fusion can lead to micron-size cracks and voids in large-area NC thin films, requiring multi-layer NC deposition to fill empty space and achieve high conductivity[30]. Nonetheless, uniform contraction and densification and micron-long continuity can be achieved in the printed NC lines after the L-E treatment when the printing morphologies are optimised. The discussion related to the morphology evolution of printed NC lines and films induced by the L-E treatment is detailed in Fig. 2. To enhance the adhesion of printed NCs on the substrates and avoid delamination after the L-E treatment, we adopt the strategy from spin-coated NC devices to pre-grow a self-assembled monolayer of (3-Mercaptopropyl)trimethoxysilane (MPTS) on the substrates for the rest of the study (see 'Methods').

Therefore, this L-E-assisted EHDP approach enables room-temperature printing assembly of NCs into dense sub-micron solids of electronically coupled NCs. The printed lines and films of Ag NCs and PbS NCs achieve optoelectronic properties comparable to those of

spin-coated counterparts, whose mechanisms and optimisation will be discussed in length in the following sections. Besides Ag and PbS NCs, the L-E-assisted nano-printing is generally applicable to other NC inks, including semiconductive CdSe NCs and InSb NCs, and dielectric ZnO NCs, showcased with the NH_4SCN and EDT L-E to realise various pattern designs at sub-micron resolution, promoting multi-material printing capabilities (Figs. 1l and S3).

Forming continuous lines with connected NCs is essential to ensure electrical and optoelectronic properties in 1D and 2D functional structures. Using Ag NC inks with NH_4SCN L-E as a model system, we investigate the effect of printing parameters, namely the stage speed υ and pulse voltage V, on determining the printed line morphologies with a fixed nozzle outer diameter of 2 μm. Semiconductive Si with thin native SiO_2 layers is used as the substrate to avoid leveraging the autofocusing effect observed on highly conductive metal substrates and the repulsion effect caused by charged particles printed on insulating substrates, both of which alter the morphology of printed lines. We also include the impact of printing parameters for depositing Ag NCs on insulating SiO_2 substrates in Fig. S4, offering guidelines for printing NC-based electronic and optoelectronic devices.

We print a series of line arrays with the same Ag NC ink to study the influence of υ and V on the amount of Ag NC deposition per unit printing length by SEM and EDX characterisation (Fig. S5 and Supplementary Text 2). According to the amount of deposited Ag NCs per unit length, we observe three modes of morphology transformation upon removal of all organic ligands and NC fusion by the NH_4SCN L-E treatment on printed Ag NCs. As shown in the top row of Fig. 2a, when the υ is low, and the V is high, printed Ag NC lines are thick and wide. L-E of these structures causes a significant volume shrink to form nanopores inside and on the surface. In contrast, too fast υ and too low V result in insufficient Ag NC deposition to compensate for voids generated by the L-E process, leading to crack formation in the NC film (Fig. 2a, bottom). Therefore, optimal printing parameters exist when Ag NC lines become densified along the direction perpendicular to the printing direction, i.e., along the width of the lines, after L-E without leaving behind pores or cracks. The SEM images in Figs. 2a and-S6 and S7 show that the finest linewidth of 70 nm can be reached for continuous Ag NC lines by the L-E-assist nano-printing on semiconductive Si substrates (see 'Methods'). Also, the quartic fractal Hilbert curve of 50 × 50 μm^2 in size (Fig. 2b) and other fractal order curves of 150 × 150 μm^2 in size (Fig. S9) have been printed to demonstrate the continuity and integrity of L-E-treated Ag NC lines. The curve patterns are one-off printed with a uniform linewidth of 550 nm and a thickness of less than 100 nm over straight paths and 90° turns.

To further understand the correlation between printed line width and height before and after L-E, we select and analyse Ag NC lines printed at 350 V with different υ. As depicted in Fig. 2c, the linewidth decreases with the increase of υ, as the number of ink droplets as well as the deposited amount of Ag NCs per unit length decreases. The L-E treatment further shrinks the linewidth, as consistently shown in SEM images, but the relative dimension change varies with υ. When υ is over 6.0 μm/s, the linewidth of as-printed Ag NCs is less sensitive to the speed change, and the decrease caused by L-E is smaller due to the insufficient amount of Ag NCs to migrate and fuse, corresponding to the third mode in Fig. 2a. Similarly, the line height also decreases as υ increases (Fig. 2d). The reduction in line height after L-E is less than 10% for structures printed slower than 2.5 μm/s. The height difference increases and becomes approximately constant as υ exceeds 4.0 μm/s, indicating the transition of deformation modes described in Fig. 2a.

Since the line width and height can be modified differently by L-E, it is necessary to statistically investigate the aspect ratio (line height/width, H/W) after L-E relative to that before L-E, namely relative aspect ratio (RH/W). $RH/W = 1$ represents the Ag NC line is shrunk isotopically in width and height, while $RH/W < 1$ (or $RH/W > 1$) means the height (or width) is reduced more than the width (or height). Based on the analysis of Fig. 2c, d, RH/W is a function of both υ and V. We only plot the points where the RH/W is greater than 0.8 to highlight the transition point (Fig. 2e). The transition point of $RH/W \approx 1$ shifts first to lower and then to higher υ as V rises from 250 V to 600 V, indicating alterations in the EHDP mode (Supplementary Text 3). This RH/W analysis provides a detailed reference for parameter selection to guide topography-specific printing fabrication.

Printing gapless arrays of lines to form crack-free thin films is the next critical step for building optoelectronic devices. We print NCs while moving the stage forwards and backwards with a spacing between two parallel lines (Fig. S10a). As-printed NC lines are non-conductive with limited dielectric constants, disrupting the surrounding electric field distribution to impede further printing of subsequent lines. Therefore, the spacing between neighbouring printed lines and the width of printed lines should be designed cohesively to minimise interline interference but achieve high packing density of the line arrays and, hence, high filling ratios (FRs) of the printed Ag NC film. The printing parameters for NC films need to be adjusted accordingly from those for NC lines.

Since organic ligands are removed after the L-E process, the FR of printed films is the area taken by bare NCs over the total printing area. With the same interline spacing, the FR is again governed by υ and V. Additionally, multiple NC layers can be printed along slightly offset traces within the same area to enhance the packing density (Fig. S10b). We define an effective speed $\upsilon_e = \upsilon/l_N$, where l_N represents the number of printed layers to be correlated with the total amount of NCs deposited per unit time. By analysing the relative area of Ag to the total printing area in SEM images, we calculate FRs of NH_4SCN-treated Ag NC films printed in the jetting mode (Fig. S11a). It shows a linear decrease from 75 ± 5% to 20 ± 1% as υ_e increases from 2.5 to 10.5 μm/s (Fig. S11b). If every deposited NC layer contributes equally to the FR, the relative FR is expected to have an inversely proportional relation to υ_e (Fig. S11b). However, the measured FR is higher than the calculated relative FR, especially at intermediate υ_e. This deviation suggests that the first Ag NC layer, although printed with high υ, is sufficiently dense to sustain a high FR, such that fewer additional layers are needed or higher υ_e is allowed to obtain the same high FR.

The pulse voltage V is also critical for the morphology and FR of printed Ag NC films. With a constant υ_e of 5.0 μm/s, when V is close to the threshold voltage to trigger ejection, the as-printed film contains a substantial portion of voids and becomes microporous after L-E (Fig. 2f, g, top). With such a low V, the width of printed lines is narrower than the spacing of 400 nm between them, leaving unfilled space. Meanwhile, the volume shrink created by organic ligand removal and Ag NC sintering cannot be compensated due to limited overall Ag NC content. The resulting cross-linked Ag NC network is highly porous with a low FR of less than 10%. Increasing V from 250 V to 650 V smooths the printed Ag NC film with fewer pores, owing to broader linewidth and higher Ag NC content per printed area (Fig. 2f, g, middle). However, when V is so high that excessive Ag NCs are printed per unit length, we observe wavy surface structures from the printed Ag NC film after L-E, where 5-μm wide cracks are formed longitudinally along the printing direction (Fig. 2f, g, bottom). This phenomenon is consistent with spin-coated thick NC films reported previously[31]. The quantitative relationship between V and FR is investigated with υ_e and interline spacing fixed at 5.0 μm/s and 400 nm, respectively. As shown in Fig. 2h, the FR of as-printed Ag NC film increases with V and reaches unity beyond V = 550 V. However, after the NH_4SCN L-E treatment, the FR increases monotonically when V changes from 250 V to 650 V, but starts to drop when V is larger than 650 V, consistent with the description in Fig. 2f. Our goal is to print thin films with high uniformity and FRs but minimum thickness that are desirable for multi-layer printing to avoid stair-step effects[22]. In addition, we systematically investigate υ_e and other printing parameters for different ligand reagents to improve the uniformity and reduce cracks of printed PbS thin films (Fig. S12).

https://doi.org/10.1038/s41467-025-64596-4

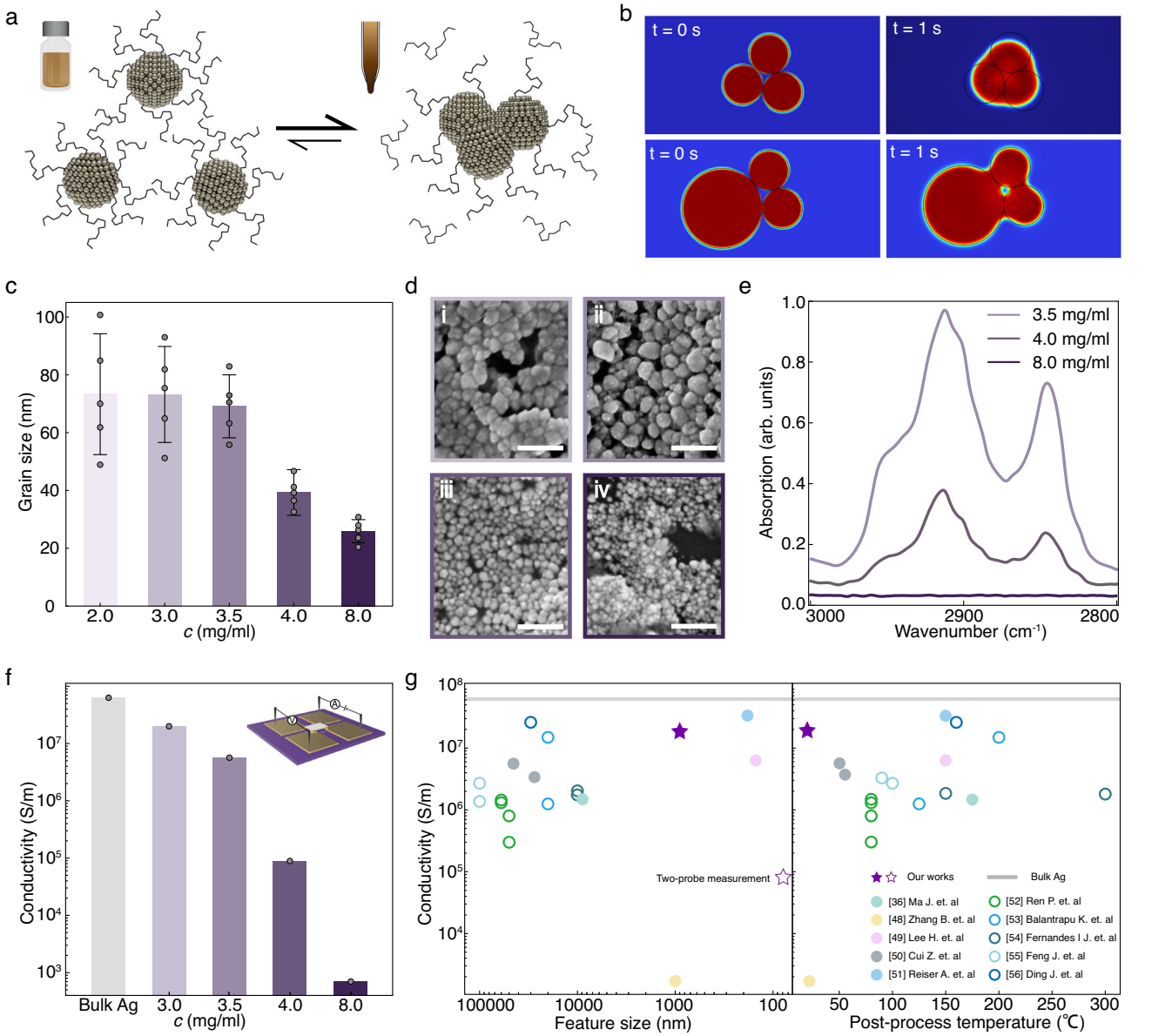

Fig. 3 | Effects of Ag NC ink concentration on L-E-induced post-printing grain growth. a Illustration of ligand detachment from the NC surface occurring near the nozzle tip with locally increased ink concentration. **b** Finite element method (FEM) simulation of L-E induced NC fusion process with different-sized NCs (small: large diameters = 1:3) without ($t = 0$) and with the L-E process ($t = 1\,s$). **c** Grain sizes and **d** SEM images of Ag NC films printed with various ink concentrations, including (i) 2.0 mg/ml, 3.0 mg/ml, (ii) 3.5 mg/ml, (iii) 4.0 mg/ml, and (iv) 8.0 mg/ml, and treated by NH_4SCN L-E. Scale bars: 100 nm. (Error bars represent standard deviation of $n = 5$ independent measurements). **e** Nano-FTIR absorption spectrum of printed Ag NC films with 3.5, 4.0, and 8.0 mg/ml ink concentrations and after the same NH_4SCN L-E treatment. **f** 4PP DC conductivity of Ag NC films printed with 3.0 to 8.0 mg/ml ink concentrations after NH_4SCN L-E and the $NaBF_4$ treatment. **g** Comparison of DC conductivity, achievable feature sizes, and post-processing temperatures of printed Ag NC inks in the literature by EHDP[36,48–51] and inkjet printing[52–56]. The solid-star is measured by the 4PP from a printed Ag NC film of $1 \times 1\,\mu m^2$ and the open-star is measured by the two-probe method from a printed single Ag NC line of ~80 nm linewidth. The solid line represents the bulk Ag conductivity.

Room-temperature chemical sintering of EHDP Ag NCs

L-E treatments with compact ligands cause chemical sintering and grain growth of NCs, leading to high conductivity in spin-coated Ag NC films[12]. Applying the chemical treatment on nano-printed NC structures, we find the L-E-induced grain size evolution is more sensitive to the ink concentration used in the EHDP process. Five different ink concentrations, including 2.0 mg/ml, 3.0 mg/ml, 3.5 mg/ml, 4.0 mg/ml, and 8.0 mg/ml, are used to print Ag NC films of $50 \times 30\,\mu m^2$. They experience the identical NH_4SCN L-E post-treatment, but the averaged grain size extracted from SEM images decreases from 73.3 ± 20.9 nm to 25.9 ± 4.0 nm when the NC ink concentration increases from 2.0 mg/ml to 8.0 mg/ml (Fig. 3c, d). The variation in grain sizes originates from different thermodynamic driving forces and kinetic rates of chemical fusion and grain growth of NCs, which are shown to be modulated by NC-ligand bonds and particle sizes before L-E[29].

Compared to polymer matrix encapsulated metal NCs and nanoparticles in previous EHDP studies[20,32], the organic ligand coordination on the NC surface is in a dynamic balance and less stable[33]. To investigate the effect of the EHDP process on NC surface ligands, we employ nano-FTIR to probe the remaining organic ligands on printed Ag NC films. As the ink concentration becomes higher, increasingly small C-H signals are detected from as-printed Ag NC films (Fig. 3e). With an ink concentration of 4.0 mg/ml, near-zero IR absorption of the C-H

fingerprint is spotted at larger aggregation sites formed in as-printed Ag NC films. The IR absorption intensity becomes undetectable from the entire surface of Ag NC films when printed with an 8.0 mg/ml ink. These observations suggest that the EHDP process causes detachment of organic ligands at high NC concentrations. As illustrated in Fig. 3a, a portion of the organic ligands could leave the NC surface when NCs are squeezed closer together in highly concentrated NC inks[33], leading to irreversible NC agglomeration. This process is even facilitated by solvent evaporation and high electric field strength to concentrate NCs locally at the nozzle tip. The ligand detachment could also occur during sessile droplet evaporation, as the stripped or loosely bonded organic ligands move in opposite directions as the aggregated NCs along the electric field lines[34].

Based on our previous studies, the L-E of organic ligands by compact ligands reduces interparticle distance and exposes high-energy surfaces, driving the fusion of NCs[29]. Upon L-E with NH_4SCN, surface Ag atoms can diffuse across Ag NCs to grow larger grains without the OA shell hindrance. However, the grain size is limited to ~100 nm, consistent with our observation (Fig. 2c) and a recent study[35]. Smaller NC diameters favour the fusion and grain growth process[36]. Here, we describe the L-E-induced chemical sintering process using the Allen-Cahn equation used for particle coalescence modelling[37], where the specific surface area (SSA, surface area/volume) determines the diffusion coefficient of Ag atoms and available free energy released by the L-E process. The SSA of agglomerated particles (~200 nm) found in printed NCs from concentrated inks is reduced by about 50 times that of original Ag NCs (~4 nm). Consistently, the numerical simulation of this model shows particles with small diameters coalesced more readily than particles with 3 times larger diameters after the same L-E reaction time to yield higher packing density (Fig. 3b and Supplementary Text 4). Correlating the IR and calculation results, we conclude that substantial portions of organic ligands are lost during EHDP of high-concentration NC inks, forming bigger aggregations of Ag NCs upon printing, which provide limited driving forces for the following L-E-induced chemical sintering process.

The DC conductivity of Ag NC pads is measured by the four-point probe (4PP) method (see 'Methods'). Since the grain size increases as the ink concentration decreases, the highest conductivity is achieved when the ink concentration reaches 3.0 mg/mL (Fig. 3f). By treating the printed Ag NC film with NH_4SCN solutions at room temperature, we convert an insulating film to one with the conductivity of 1.78×10^7 S/m, which can be further improved to 1.99×10^7 S/m by briefly dipping the film in a $NaBF_4$ aqueous solution to reduce surface oxidation of Ag NCs[30]. The conductivity of printed Ag NC film ($1 \times 1\,\mu m^2$) is comparable to that of large-area spin-coated Ag NC films with the same ligand and chemical treatment[30]. We also print single Ag NC lines across two Au electrodes with a 5-μm gap on the insulating SiO_2 substrate. After the same NH_4SCN L-E treatment, the linewidth varies between ~120 nm to ~50 nm (Fig. S8), showing a conductivity of 7.5×10^4 S/m. This two-probe measurement is limited by the contact resistance between printed Ag NC lines and the Au electrode, and the non-uniform linewidth is due to the disrupted electric field near the Au electrode. However, the accurate electrical conductivity of the finest Ag NC lines with 4PP requires more advanced nano-fabrication and printing parameter optimisation, which are beyond the scope of this paper. Figure 3g separately compares the conductivity vs. feature sizes and vs. post-processing temperature achieved in this work with other printed Ag NC inks in the literature, benchmarking the low-temperature chemical sintering approach for nanoscale device applications.

Nano-optics and sub-micron electrodes based on nano-printed Ag NC lines

We exploit the nanoscale resolution and high conductivity of printed Ag NC lines to construct grating-based structural colours (SCs). The grating structure diffracts the incident white light into monochromatic lights at specific angles and phases to generate various SCs (Fig. 4a), promising in flexible display, strain sensing, and anticounterfeiting applications[38,39]. We use L-E-assisted nano-printing to fabricate Ag NC line arrays with NH_4SCN L-E on ITO/glass substrates to form grating patterns. The linewidth and pitch size of the printed Ag NC gratings can be accurately controlled by combining the printing parameter optimisation and the L-E-induced shrinking effect studied above. The resulting Ag NC gratings are precisely defined and satellite-free with an interline spacing ranging from 1900 nm to 600 nm at a 100 nm interval, generating high-purity SCs. The SEM images show printed Ag NC line gratings with 320 nm linewidth and pitches of 2220 nm, 1720 nm, and 1320 nm, respectively, to achieve RGB SCs (Fig. 4b). More SCs can be formulated by combining different pitches within one grating structure, depending on the ratio of basic RGB SC gratings, as shown in Fig. 4c. For example, white colour is observed when three primary SC gratings are printed at equal fractions. Compared with the meniscus-guided printed polymeric SCs in a recent report[39], our results obtain a wider colour gamut (Fig. 4d), attributing to smaller linewidth and more tunable line spacings. They are also compatible with high printing speeds of 25 μm/s.

Besides line gratings, we print Ag NCs for complex linear patterns with extended functionalities. Figure 4e, g demonstrates Ag NC electrode arrays with sub-micron feature sizes, suitable for single-cell monitoring and biomolecule sensing. Figure 4f, h shows metasurfaces consisting of subwavelength split-ring resonators simulated to resonate in the long-wavelength IR (LWIR) region (Fig. S13). We successively print these structures, including the line gratings and microelectrode arrays, on polydimethylsiloxane (PDMS) thin films to show the compatibility of this room-temperature additive manufacturing method with flexible substrates (Supplementary Movie 1).

All-printed multi-layer PbS NC IR photodetectors

IR-absorbing PbS NCs have been developed as building blocks to construct photodetectors (PDs) from the bottom up[40]. Although PbS NC IR PDs have been progressively improved by developing chemical modifications for NCs and stacking different functional layers, the pixelation of these spin-coated devices is still underexplored, especially below 100-μm pixel sizes[10]. Therefore, we utilise the L-E-assisted nano-printing to form sub-10 micron PbS NC patterns and PD devices at room temperature (see 'Methods'). To verify the optoelectronic properties of printed PbS NCs, we first compare the photoresponse of printed vs. spin-coated PbS NC films. PbS NCs with the 1st exitonic absorption peak at 1500 nm (1500 nm PbS NCs) are printed across evaporated Au electrode pairs with a 5-μm gap (Fig. 5a). The L-E treatment is performed with either EDT, TBAI, or PbI_2 solutions on printed PbS NC films, whose photocurrent spectra closely resembles those of the spin-coated PbS NC films underwent the same solid-state L-E (Fig. 5b). We note a slight red shift and broadening of the photocurrent peak for printed PbS NC films, indicating even improved electronic coupling and photocarrier delocalisation across printed NC arrays. The printed and spin-coated PbS NC photoconductors exhibit similar steady and transient photoresponse under 1480 nm illumination, as shown in Fig. S14.

The two-terminal PbS NC photoconductors are printed on degenerately doped Si with 300 nm SiO_2, which can also be operated as field-effect transistors (FETs) by adding a third gate voltage across the p^{++}-Si and one of the two electrodes (Fig. 5a). We measure the transfer characteristics of TBAI-treated printed PbS NC FETs (Fig. 5c). In the dark, it shows predominant p-type behaviour, due to air exposure of PbS NCs during the device handling and measurement[41,42]. Under illumination by a 1480 nm monochromic light, the on and off currents increase while the their on/off current ratio decreases. The higher photocurrent at $V_G = 0$ to 40 V is consistent with higher hole concentration due to photogeneration in the PbS NC channel layer. PbS NC films can also be printed on pre-printed Ag NC electrodes to form all-printed PbS NC photoconductors and their arrays (Fig. S15).

https://doi.org/10.1038/s41467-025-64596-4

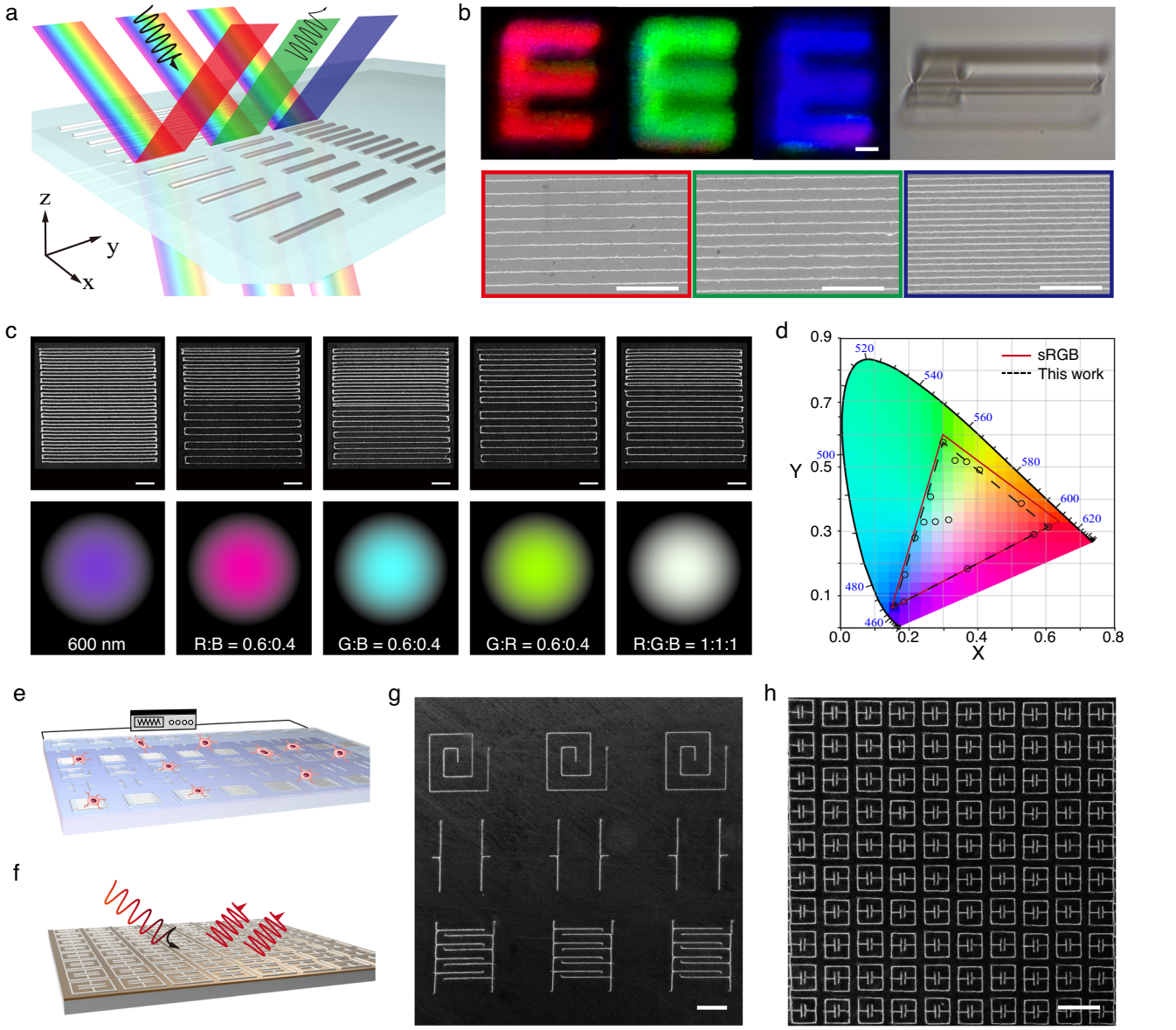

Fig. 4 | Applications of nano-printed Ag NC lines. a Illustration of structural colours (SCs) generated by grating structures. **b** Optical (top) and SEM (bottom) images of printed Ag NC RGB SCs with an 'E' shape, based on 2220 nm (left), 1720 nm (middle), and 1320 nm (right) pitch sizes, respectively. Scale bars: 10 µm. (Similar results are repeated independently for $n = 10$.) **c** SEM images of printed Ag NC gratings and their corresponding SCs formed by programming the pitch and mixing different ratios of RGB SC gratings. Scale bars: 10 µm. (Similar results are repeated independently for $n = 10$.) **d** Chromaticity coordinates of the representative SCs in **c** on a CIE 1931 chromaticity diagram. Illustration of **e** printed sub-micron electrode arrays for single-cell monitoring and **f** printed metasurfaces resonating in LWIR wavelengths. SEM images of **g** printed Ag NC sub-micron electrode arrays and **h** printed LWIR split-ring resonator metasurfaces. Scale bars: 10 µm. (Similar results are repeated independently for $n = 5$.).

Then, we further prove the feasibility of printing multi-layer PbS NCs by stacking a film of PbS NCs with a 950-nm absorption peak (950 nm PbS NCs) on top of a 1500 nm PbS NC film to construct a bilayer photoconductor. Both NC films are treated by TBAI immediately following the printing step. The photocurrent spectra show the contribution from both NC layers even though the Au electrodes are only in contact with the bottom NC film (Fig. 5e). This is consistent with the funnel effect previously reported in spin-coated PbS NC films, where the photocarriers generated in the wider-bandgap and smaller-sized NCs can migrate through the graded band alignment to reach the bottom metal contact[43]. Although the overall photocurrent is dominant by that of the 950 nm PbS NC layer when illuminated by 945-nm light as shown in Fig. 5e, the transient photoresponse of the stacked NC photoconductors is more alike that of the single-component 1500 nm PbS NC photoconductors (Fig. 5f), consistent with the carrier transport mechanism that is dominated by the bottom layer in this bottom-contact geometry. These characteristics indicate that the optoelectronic property of the bottom PbS NC film is not altered after printing the top PbS NC layers.

Encouraged by the above results, we further explore the printing of multi-layer and multi-material PbS NC IR PDs. Instead of single-layer PbS NC photoconductors, we utilise the distinct doping effect of EDT (more p-type) and TBAI (more n-type) L-E on PbS NC films to build bilayer photoconductive devices and facilitate photocarrier charge separation at the NC film interface[40,44]. Besides, Au and Ag with higher and lower work functions can be more favourable metal contacts to reduce carrier injection barriers with the EDT-treated and TBAI-treated side, respectively. Therefore, we print Ag and Au NC

https://doi.org/10.1038/s41467-025-64596-4

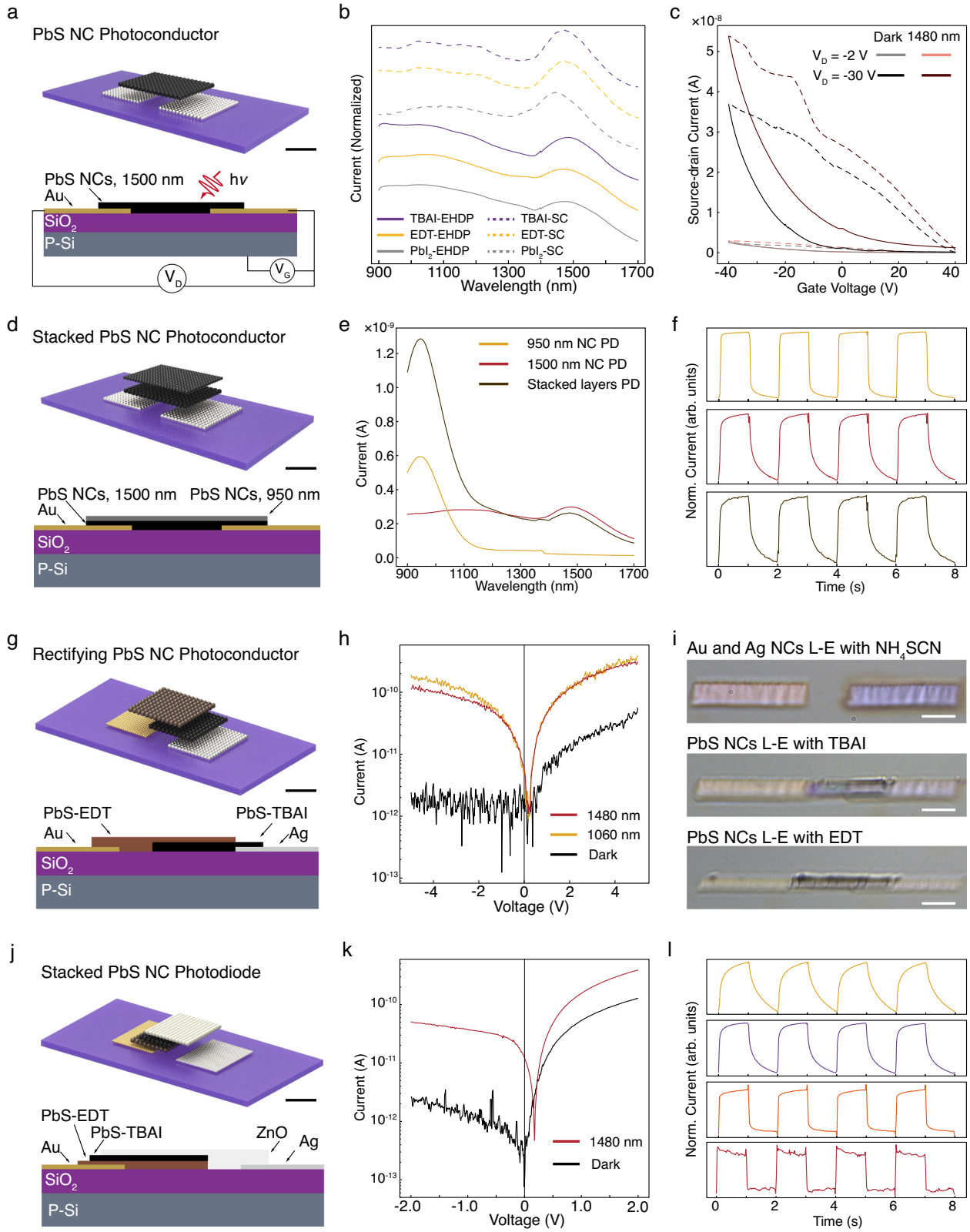

films to form bottom electrode pairs, both assisted by the NH_4SCN L-E treatment. On the Ag electrode, TBAI-treated PbS NC layers are printed, topped by EDT-treated PbS NC layers printed to connect with the Au NC electrode (Fig. 5g, i). The overlapping area of the two PbS NC layers defines the semiconductor junction with a sharp interface (Fig. S16). The final device printed with 1500 nm PbS NCs shows rectifying behaviour in the dark with a dark current as low as 3.3×10^{-11} A (Fig. 5h). In contrast, the same PbS NC stack printed on symmetric Au electrode pairs exhibits linear I-V characteristics (Fig. S17), whose electron injection and extraction are hindered by the PbS NC-TBAI/Au NC interface. The formation of solid junctions and depletion regions in the printed bilayer photoconductor also shortens the response time from about 300 ms of the single-layer devices to less than 60 ms (Fig. 5l).

Fig. 5 | Printed NC IR micro-PDs based on multi-material and multi-layer nano-printing. a Schematics of printed PbS NC IR photoconductors. Scale bars: 5 µm. **b** Normalised photocurrent of printed (solid) and spin-coated (dashed) PbS NC photoconductors with EDT (yellow), TBAI (purple), and PbI_2 (grey) L-E treatments. **c** I_D-V_G curves of printed PbS NC photo-transistors with TBAI L-E in the linear ($V_D = -2V$) and saturation ($V_D = -30$ V) regimes in the dark (black) and excited by 1480 nm light of 2.5 mW/cm^2 (red). The solid and dashed lines differentiate forward and backward scans, respectively. **d** Schematics (Scale bars: 5 µm) and **e** photocurrent of the 950 nm/1500 nm stacked (dark yellow), 950 nm (yellow), and 1500 nm (red) PbS NC photoconductors with TBAI L-E. **f** The transient photocurrent of single-component 950 nm (yellow) and 1500 nm (red) and stacked (dark yellow) PbS NC photoconductors under an applied voltage of 5 V and chopped 1480-nm light illumination at 1 Hz frequency. All currents are normalised to their respective highest photocurrent values. **g** Schematics of printed rectifying PbS NC IR photoconductors. Scale bars: 5 µm. **h** I-V characteristics of printed rectifying PbS NC IR photoconductors with 1500 nm PbS NCs in the dark (black) and under 1060 nm (yellow) and 1480 nm (red) illumination. **i** Optical microscopy images taken during the fabrication of the bilayer PbS NC IR photoconductors with asymmetric metal NC contacts. Scale bars: 10 µm. (Similar results are repeated independently for $n = 10$). **j** Schematics of the device architecture for all-printed PbS NC/ZnO NC IR photodiodes, containing sequentially printed layers of Au NC-SCN/PbS NC-EDT/PbS NC-TBAI/ZnO NC-SCN/Ag NC-SCN with respective L-E treatments. **k** I-V characteristics of all-printed 1500 nm PbS NC/ZnO NC IR photodiodes in the dark (black) and under 1480 nm illumination (red). **l** Transient photocurrents of different devices based on 1500 nm PbS NCs under 1 Hz on/off illumination with 1480-nm light (2.5 mW/cm^2) and an applied voltage of −2 V: EDT-treated PbS NC photoconductors (yellow), TBAI-treated PbS NC photoconductors (purple), PbS NC-TBAI/PbS NC-EDT rectifying photoconductors (orange), and all-printed PbS NC/ZnO NC heterojunction photodiodes (brown). All currents are normalised to their respective highest photocurrent values.

However, the bilayer structure with asymmetric metal contacts still cannot guarantee obvious open-circuit voltage under light illumination even with shorter excitation wavelengths (Fig. 5h). The device operation is dominant by the photoconductor mode over the photovoltaic mode of photodiodes. Therefore, we finally introduce ZnO NCs as the n-type electron transport layer and achieve all-printed NC photodiodes. Instead of vertically stacking active layers with at least one transparent top or bottom electrode in the typical photodiode structure, we fabricate the NC photodiodes through printing and overlapping multiple layers laterally across the two bottom metal electrodes. As shown in Fig. 5j, a pair of Au and Ag NC pads are printed with a gap and treated by SCN^- L-E. Then, layers of PbS NC-EDT/PbS NC-TBAI/ZnO NC-SCN are sequentially printed followed by respective L-E treatments, where the ZnO NC layer is deposited on top of the PbS NC layers and separate the PbS NC layers from the Ag NC electrode. As a result, the complete conduction pathway is through Au NC-SCN/PbS NC-EDT/PbS NC-TBAI/ZnO NC-SCN/Ag NC-SCN, which contains charge transport directions both horizontally within each layer and perpendicularly across junction interfaces between layers. We demonstrate such all-printed devices with pixel sizes of the photoactive area of 30×15 µm^2 and 9×9 µm^2 to be comparable with the state-of-the-art IR imager resolution (Figs. S18 and 19). With 1500 nm PbS NCs, the all-printed NC photodiode shows rectifying IV characteristics with a low dark current of 2.1×10^{-12} A. Under 1480 nm light illumination, the device achieves an open-circuit voltage of 0.2 V and an EQE of 56.1% at −4 V (Table S2 and Fig. 5k). The relatively high EQE is also attributed to the direct illumination on PbS NC layers without the absorption loss in transparent top electrodes[45]. The built-in electric field formed in the photodiode device facilitates charge separation and leads to further reduction in the response time to less than 20 ms (Fig. 5l), which is beyond the time resolution of our instrument.

We develop a general method to pattern and chemically modify NC structures through layer-by-layer printing. Compared to conventional inkjet printing and high-temperature post-sintering, our method takes advantage of the nano-resolution EHDP and room-temperature L-E processes to diversify the variety of NC ink properties, substrate compatibility, and printed microelectronics functionality. From the model study on Ag NCs, we systematically investigate each printing parameter and establish the L-E-assisted sintering mechanism. The dynamic NC-ligand coordination during printing is found to determine the driving force for the chemical fusion of NCs. We further verify the semiconductor properties of printed PbS NCs and assemble all-printed multi-layer photodiode devices with photoresponse to ~1500-nm-wavelength irradiation. The diode performance is enhanced by asymmetric metal electrodes, whose fabrication is more facile and flexible by printing different metal NCs than by metallisation after repetitive lithographic processes. While 3D integration and hybrid electronics are proposing solutions to realising sensing, communication, computing, and more in a single device[22,46], this chemical-assisted nano-printing method offers versatile and practical approaches to addressing the key challenge of hetero-material and hetero-device integration on both rigid and flexible substrates.

Methods

Ink, nozzle, and substrate preparation

The chemicals and synthesis recipes of colloidal NCs are described in the Supplementary Information. The Ag NC ink is prepared by dispersing Ag NCs in dodecane (Supplementary Text 1) with concentrations varied from 2.0 mg/ml to 8.0 mg/ml. The Ag NC ink is sonicated for 5 min at 25 °C before loading into the nozzle. The Au, 1500 nm PbS, 950 nm PbS, CdSe, and ZnO NC inks are prepared in the same way as the Ag NC ink with a concentration of 6.0 mg/ml, 3.0 mg/ml, 4.0 mg/ml, 4.0 mg/ml, and 20.0 mg/ml, respectively.

The capillary nozzles with 2–4 µm outer diameters are made using the Micropipette Puller (Sutter P-97) by setting the heating temperature and pulling speeds.

The rigid substrates, including SiO_2, Si, Au-coated Si/SiO_2, and ITO-coated glass, are ultrasonically cleaned in isopropyl alcohol for 5 min. The cleaned substrates are further treated in an oxygen plasma at 100 W and 0.5 mbar for 1 min or 20 s if the substrate is coated by Au. Then, the substrates are soaked in (3-mercaptopropyl)trimethoxysilane (MPTS)/toluene solution (5 vol%) for 6 h and ultrasonically cleaned in ethanol for 5 min after rinsed by toluene. This pre-process has been demonstrated to improve the adhesion force between NCs patterns and substrates. The Au electrodes consisting of 10 nm Cr and 50 nm Au are thermally evaporated through shadow masks on the Si substrate with a 300 nm SiO_2 layer. For flexible substrates, the PDMS film with a thickness of 50 µm is fixed onto the surface of Au-coated Si wafers and peeled off after EHDP.

Ligand-exchange (L-E) treatment

The ligand reagent NH_4SCN powders are dissolved in methanol to form a solution with 1 mg/ml concentration. As soon as the EHDP process is finished, 80 µL of the NH_4SCN solution is applied to cover the printed patterns with a micropipette. After 60 s, the residual ligands are washed away from the printed area with pristine methanol. The L-E process of TBAI, PbI_2, and EDT is similar to that of NH_4SCN, where the concentration of the TBAI methanolic solution is 1 mg/ml, the EDT solution is 0.005% vol% diluted with acetonitrile (ACN), and the concentration of the PbI_2 solution is 2 mg/ml in N,N-dimethylformamide (DMF).

Characterisations

The SEM images and EDX characterisation are taken with a Hitachi S4800 field emission SEM equipped with two secondary electron detectors. The nano-FTIR spectra are collected by Bruker Anasys nanoIR3, and the data are processed with Analysis Studio Bruker software. The AFM measurements are performed by the Bruker

Dimension Icon AFM instrument in tapping mode. The second-order flatten and the plane fit processing of the data are carried out with NanoScope Analysis, Bruker. The full width and height at the quarter maximum of the AFM profile are extracted as the line width and height.

Filling-ratio (FR) calculation

The top-view SEM images of printed Ag NC films are processed by ImageJ to enhance the contrast. Then, a self-developed Python code is used to calculate the percentage of pixels containing Ag as the FR. The FR of each sample takes the average value calculated from ten different areas of that sample.

Electrical measurement of Ag NC films

Four-point probe conductivity is measured using four Au electrodes defined by direct laser writing (Picomaster 200) and thermal evaporation to form a 2 × 2 array with 5 µm gaps between them. Ag NC films (20 µm × 20 µm) are printed onto the centre of the four-electrode pair to ensure adequate contact area between the sample and electrodes. The sample is tested after the L-E process with 1 mg/ml NH4SCN solution for 60 s, and measured again after further reduction by 25 mM $NaBH_4$ aqueous solution for 90 s. The four-point probe conductivity measurement is carried out with a probe station (CHPUIST ZH-4) and source meter (Keysight B2902B). The sheet resistance R_S is calculated according to the Van der Pauw equation[47]:

$$e^{-\pi R_{12,34}/R_s} + e^{-\pi R_{23,41}/R_s} = 1 \quad (1)$$

where the $R_{12,34}$ is calculated by V_{34}/I_{12}, in which V_{34} is the voltage drop between Au electrodes 3 and 4 when the current I_{12} is applied between Au electrodes 1 and 2. The same nomenclature format applies for $R_{23,41}$.

Field-effect transistor (FET) devices are characterised using a standard three-terminal setup. Two probes are in contact with source and drain electrodes interfaced with the NC channel layer, and a third probe is applied on the degenerately p-doped Si common gate for the gate bias. A probe station (CHPUIST ZH-4) and source meter (Keysight B2902B) are employed for FET measurements.

Structure colour (SC) characterisation

The printed SCs are imaged by a self-built apparatus composed of a collimated white LED light source (XH-PTI025-5V, Xinheng high-tech), a colour camera (Blackfly U3, FLIR), and a 2X infinity-corrected objective lens (FL = 100.0 mm, NA = 0.055, Mitutoyo). The light source is fixed at a 45-degree incident angle to the printed SCs, and the objective lens is located in the normal direction above the sample to receive the diffracted light.

Photoresponse measurement of printed PbS NC devices

The photocurrent of printed PbS devices is measured with an IR probe station (DSR600, Zolix Instruments) under −5V to 5 V bias with scanning wavelengths or a single wavelength excitation. The monochromic excitation wavelength used for PbS NC photodetectors includes 1060 nm (1.7 mW/cm^2) and 1480 nm (2.5 mW/cm^2). Transient photoresponse is collected by chopping the illumination light source with an optical shutter at 1 Hz and monitoring the current with a semiconductor parameter analyser (Keysight B1500A). The external quantum efficiency (EQE) is calculated using the equation below:

$$\mathrm{EQE}(\lambda) = \frac{I_{ph} \cdot hc}{q \cdot P_{opt} \cdot \lambda} \quad (2)$$

where I_{ph} is the photocurrent, h is Planck's constant ($6.626 \times 10^{-34}\,Js$), c is the light speed, q is the elementary charge ($1.602 \times 10^{-19}\,C$), P_{opt} is the incident optical power, and λ is the wavelength of the incident light.

Reporting summary

Further information on research design is available in the Nature Portfolio Reporting Summary linked to this article.

Data availability

The data that support the findings of this study are present in the paper and/or in the Supplementary Information. Additional data related to the paper are available from the corresponding author upon request. Source data are provided with this paper.

References

1. Luo, Y. et al. Technology roadmap for flexible sensors. *ACS Nano* **17**, 5211–5295 (2023).
2. Huang, T.-Y., Gu, H. & Nelson, B. J. Increasingly intelligent micromachines. *Annu. Rev. Control Robot. Auton. Syst.* **5**, 279–310 (2022).
3. Song, M. et al. 3D microprinting of inorganic porous materials by chemical linking-induced solidification of nanocrystals. *Nat. Commun.* **14**, 8460 (2023).
4. Zeng, M. et al. High-throughput printing of combinatorial materials from aerosols. *Nature* **617**, 292–298 (2023).
5. Somers, P. et al. The physics of 3D printing with light. *Nat. Rev. Phys.* https://doi.org/10.1038/s42254-023-00671-3 (2023).
6. Saha, S. K. et al. Scalable submicrometer additive manufacturing. *Science* **366**, 105–109 (2019).
7. Duan, Y., Xie, W., Yin, Z. & Huang, Y. Multi-material 3D nanoprinting for structures to functional micro/nanosystems. *Int. J. Extrem. Manuf.* **6**, 063001 (2024).
8. Xiao, Z. et al. Solution-processed quantum dot micropatterns: from liquid manipulation to high-performance quantum dot light-emitting diode devices. *ACS Nano* **19**, 10609–10619 (2025).
9. Mu, G. et al. Visible to mid-wave infrared PbS/HgTe colloidal quantum dot imagers. *Nat. Photon.* https://doi.org/10.1038/s41566-024-01492-1 (2024).
10. Kara, G. et al. Scaling of hybrid QDs-graphene photodetectors to subwavelength dimensions. *ACS Photonics* https://doi.org/10.1021/acsphotonics.3c01759 (2024).
11. Liu, M. et al. Colloidal quantum dot electronics. *Nat. Electron.* **4**, 548–558 (2021).
12. Choi, J.-H. et al. Exploiting the colloidal nanocrystal library to construct electronic devices. *Science* **352**, 205–208 (2016).
13. Brus, L. E. A simple model for the ionization potential, electron affinity, and aqueous redox potentials of small semiconductor crystallites. *J. Chem. Phys.* **79**, 5566–5571 (1983).
14. Boles, M. A., Ling, D., Hyeon, T. & Talapin, D. V. Erratum: The surface science of nanocrystals. *Nat. Mater.* **15**, 364 (2016).
15. Jung, W. et al. Three-dimensional nanoprinting via charged aerosol jets. *Nature* **592**, 54–59 (2021).
16. Liu, B. et al. Metal 3D nanoprinting with coupled fields. *Nat. Commun.* **14**, 4920 (2023).
17. Han, F. et al. Three-dimensional nanofabrication via ultrafast laser patterning and kinetically regulated material assembly. *Science* **378**, 1325–1331 (2022).
18. Wang, Y., Yi, C., Tian, W., Liu, F. & Cheng, G. J. Free-space direct nanoscale 3D printing of metals and alloys enabled by two-photon decomposition and ultrafast optical trapping. *Nat. Mater.* https://doi.org/10.1038/s41563-024-01984-z (2024).
19. Li, F. et al. 3D printing of inorganic nanomaterials by photochemically bonding colloidal nanocrystals. *Science* **381**, 1468–1474 (2023).
20. Galliker, P. et al. Direct printing of nanostructures by electrostatic autofocussing of ink nanodroplets. *Nat. Commun.* **3**, 890 (2012).
21. Schneider, J. et al. Electrohydrodynamic nanodrip printing of high aspect ratio metal grid transparent electrodes. *Adv. Funct. Mater.* **26**, 833–840 (2016).

22. Goh, G. L., Zhang, H., Chong, T. H. & Yeong, W. Y. 3D printing of multilayered and multimaterial electronics: a review. *Adv. Electron. Mater.* **7**, https://doi.org/10.1002/aelm.202100445 (2021).
23. Ling, S. et al. Tension-driven three-dimensional printing of free-standing Field's metal structures. *Nat. Electron.* https://doi.org/10.1038/s41928-024-01207-y (2024).
24. Grotevent, M. J. et al. Nanoprinted quantum dot–graphene photodetectors. *Adv. Opt. Mater.* **7**, https://doi.org/10.1002/adom.201900019 (2019).
25. Grotevent, M. J. et al. Colloidal HgTe quantum dot/graphene phototransistor with a spectral sensitivity beyond 3 microm. *Adv. Sci.* **8**, 2003360 (2021).
26. Mester, L., Govyadinov, A. A., Chen, S., Goikoetxea, M. & Hillenbrand, R. Subsurface chemical nanoidentification by nano-FTIR spectroscopy. *Nat. Commun.* **11**, 3359 (2020).
27. Ferraresi, L. J. A. et al. AFM-IR of electrohydrodynamically printed PbS quantum dots: quantifying ligand exchange at the nanoscale. *Nano Lett.* **24**, 10908–10914 (2024).
28. Fafarman, A. T. et al. Air-stable, nanostructured electronic and plasmonic materials from solution-processable, silver nanocrystal building blocks. *ACS Nano* **8**, 2746–2754 (2014).
29. Xu, J. et al. Chemically driven sintering of colloidal Cu nanocrystals for multiscale electronic and optical devices. *ACS Nano* **18**, 17611–17621 (2024).
30. Kim, H. et al. Chemically designed metallic/insulating hybrid nanostructures with silver nanocrystals for highly sensitive wearable pressure sensors. *ACS Appl. Mater. Interfaces* **10**, 1389–1398 (2018).
31. Luther, J. M. et al. Structural, optical, and electrical properties of self-assembled films of PbSe nanocrystals treated with 1,2-ethanedithiol. *ACS Nano* **2**, 271–280 (2008).
32. Onses, M. S., Sutanto, E., Ferreira, P. M., Alleyne, A. G. & Rogers, J. A. Mechanisms, capabilities, and applications of high-resolution electrohydrodynamic jet printing. *Small* **11**, 4237–4266 (2015).
33. Morris-Cohen, A. J., Vasilenko, V., Amin, V. A., Reuter, M. G. & Weiss, E. A. J. A. Model for adsorption of ligands to colloidal quantum dots with concentration-dependent surface structure. *ACS Nano* **6**, 557–565 (2012).
34. Galliker, P., Schneider, J., Ruthemann, L. & Poulikakos, D. Open-atmosphere sustenance of highly volatile attoliter-size droplets on surfaces. *Proc. Natl. Acad. Sci. USA* **110**, 13255–13260 (2013).
35. Zheng, J. et al. A bottom-up understanding of the ligand-dominated formation of metallic nanoparticle electrodes with high broadband reflectance for enabling fully solution-processed large-area organic solar cells. *Energy Environ. Sci.* **16**, 3770–3780 (2023).
36. Ma, J. et al. Electrohydrodynamic printing of ultrafine and highly conductive Ag electrodes for various flexible electronics. *Adv. Mater. Technol.* **8**, https://doi.org/10.1002/admt.202300080 (2023).
37. Kuruganti, T., Joshi, P. K. & Goswami, M. Simulation of two nanoparticle melting to understand the conductivity drop of 3D-printed silver nanowires. *Mater. Des.* **236**, https://doi.org/10.1016/j.matdes.2023.112502 (2023).
38. Sahu, R. R. et al. Single-step fabrication of liquid gallium nanoparticles via capillary interaction for dynamic structural colours. *Nat. Nanotechnol.* https://doi.org/10.1038/s41565-024-01625-1 (2024).
39. Bae, J. et al. Three-dimensional printing of structural color using a femtoliter meniscus. *ACS Nano* **17**, 13584–13593 (2023).
40. Deng, Y. H. et al. Short-wave infrared colloidal QD photodetector with nanosecond response times enabled by ultrathin absorber layers. *Adv. Mater.* e2402002, https://doi.org/10.1002/adma.202402002 (2024).
41. Oh, S. J. et al. Selective p- and n-doping of colloidal PbSe nanowires to construct electronic and optoelectronic devices. *ACS Nano* **9**, 7536–7544 (2015).
42. Voznyy, O. et al. A charge-orbital balance picture of doping in colloidal quantum dot solids. *ACS Nano* **6**, 8448–8455 (2012).
43. Kim, J. Y. et al. Single-step fabrication of quantum funnels via centrifugal colloidal casting of nanoparticle films. *Nat. Commun.* **6**, 7772 (2015).
44. Chuang, C. H., Brown, P. R., Bulovic, V. & Bawendi, M. G. Improved performance and stability in quantum dot solar cells through band alignment engineering. *Nat. Mater.* **13**, 796–801 (2014).
45. Chehaibou, B. et al. The complex optical index of PbS nanocrystal thin films and their use for short wave infrared sensor design. *Nanoscale* **14**, 2711–2721 (2022).
46. Tan, H. W., Choong, Y. Y. C., Kuo, C. N., Low, H. Y. & Chua, C. K. 3D printed electronics: processes, materials and future trends. *Prog. Mater. Sci.* **127**, https://doi.org/10.1016/j.pmatsci.2022.100945 (2022).
47. Ramadan, A. A., Gould, R. D. & Ashour, A. On the Van der Pauw method of resistivity measurements. *Thin Solid Films* **239**, 272–275 (1994).
48. Zhang, B. et al. One-step sub-micrometer-scale electrohydrodynamic inkjet three-dimensional printing technique with spontaneous nanoscale joule heating. *ACS Appl. Mater. Interfaces* **9**, 29965–29972 (2017).
49. Lee, H. et al. On-demand 3D printing of nanowire probes for high-aspect-ratio atomic force microscopy imaging. *ACS Appl. Mater. Interfaces* **12**, 46571–46577 (2020).
50. Cui, Z., Han, Y., Huang, Q., Dong, J. & Zhu, Y. Electrohydrodynamic printing of silver nanowires for flexible and stretchable electronics. *Nanoscale* **10**, 6806–6811 (2018).
51. Reiser, A. et al. Multi-metal electrohydrodynamic redox 3D printing at the submicron scale. *Nat. Commun.* **10**, 1853 (2019).
52. Ren, P. & Dong, J. Direct electrohydrodynamic printing of aqueous silver nanowires ink on hydrophobic substrates for flexible and stretchable electronics. *Manuf. Lett.* **33**, 161–166 (2022).
53. Balantrapu, K., McMurran, M. & Goia, D. V. Inkjet printable silver dispersions: effect of bimodal particle-size distribution on film formation and electrical conductivity. *J. Mater. Res.* **25**, 821–827 (2011).
54. Fernandes, I. J. et al. Silver nanoparticle conductive inks: synthesis, characterization, and fabrication of inkjet-printed flexible electrodes. *Sci. Rep.* **10**, 8878 (2020).
55. Feng, J., Xing, B. & Xu, J. Conductivity enhancement of Ag nanowire ink by decorating in situ formed Ag particles under low-temperature sintering. *Nanotechnology* **35**, 175706 (2024).
56. Ding, J. et al. Preparing of highly conductive patterns on flexible substrates by screen printing of silver nanoparticles with different size distribution. *Nanoscale Res. Lett.* **11**, 412 (2016).

Acknowledgements

The authors thank the support from Dr. Pengfei Yang (HKU) and Jing Liu (Tsinghua-Shenzhen) for AFM measurements, Baohua Li (Tsinghua-Shenzhen) for nano-FTIR measurements, Dr. Haiyun Ma and Qiyu Cao for supplying NC inks, Dr Nanlin Zhang and Yang-Ming Quantum Tech Ltd. for supplying ZnO NC inks. The authors thank the support from the Early Career Scheme (grant 27210623, awardee: T.Z.) and General Research Fund (grant 17214024, awardee: T.Z.) of Research Grants Council of University Grants Committee, Hong Kong SAR, National Youth Science Fund (grant 62304191, awardee: T.Z.) of National Natural Science Foundation of China, and the support from the National Research Foundation of Korea (NRF) grant funded by the Korea government (MSIT) (No. RS–2025-00556379, RS–2024-00407084, awardee: J.T.K. and RS-2024-00438059, awardee S.J.O).

Author contributions

Z.Z. and T.Z. conceived the idea and wrote the manuscript. Z.Z. developed the printing methods and simulations and fabricated all printing samples. R.A. measured the electrical properties of the printed devices. Y.L. assisted with the EHD printer modification. B.K.J. and J.H.A. synthesised NCs. N.Y. fabricated metal electrodes. G.W. assisted with the nano-FTIR measurements and analysis. W.C.H.C. supported the SC measurements. L.J.L. supported the photodetector fabrication and data analysis. S.J.O. supported the ink preparation and optoelectronic measurements. J.T.K. and T.Z. co-supervised the project. All authors have edited and agreed on the manuscript.

Competing interests

The authors declare no competing interests.

Additional information

Supplementary information The online version contains supplementary material available at https://doi.org/10.1038/s41467-025-64596-4.

Correspondence and requests for materials should be addressed to Ji Tae Kim or Tianshuo Zhao.

Peer review information *Nature Communications* thanks J Devin MacKenzie and the other, anonymous, reviewer(s) for their contribution to the peer review of this work. A peer review file is available.